Algorithms for the computation of the Minkowski functionals of deterministic and random polyconvex sets

R. Guderlei [a,1], S. Klenk [b], J. Mayer [a], V. Schmidt [b], E. Spodarev [b,*]

[a] *Universität Ulm, Abteilung Angewandte Informationsverarbeitung, D-89069 Ulm, Germany* [2]

[b] *Universität Ulm, Abteilung Stochastik, D-89069 Ulm, Germany* [3]

Abstract

We give algorithms for the simultaneous computation of the area, boundary length and connectivity (the so–called *Minkowski functionals*) of binary images. It is assumed that a binary image is a discretization of a two–dimensional *polyconvex* set which is a union of convex components. Edge–corrected versions of these algorithms are used for the estimation of specific intrinsic volumes of a stationary random closed set from a single realization given by a binary image. Performance and exactness of the algorithms in two dimensions are discussed on numerical examples. Comparison to other known methods is provided.

Key words: binary image, intrinsic volume, quermaßintegral, Minkowski functional, area, boundary length, Euler–Poincaré characteristic, stationary random closed set, random field, volume fraction, Steiner formula, principal kinematic formula, parallel set.
AMS Subject Classification 2000: Primary 62H35; Secondary 60D05, 62M40, 68W01.

* Corresponding author.
Email addresses: ralph.guderlei@uni-ulm.de (R. Guderlei), simone.klenk@uni-ulm.de (S. Klenk), johannes.mayer@uni-ulm.de (J. Mayer), volker.schmidt@uni-ulm.de (V. Schmidt), evgueni.spodarev@uni-ulm.de (E. Spodarev).

[1] Research supported by the Deutsche Forschungsgemeinschaft in the research training group "Modellierung, Analyse und Simulation in der Wirtschaftsmathematik"

[2] http://www.mathematik.uni-ulm.de/sai

[3] http://www.mathematik.uni-ulm.de/stochastik

1 Introduction

Minkowski functionals such as the volume, the surface area and the Euler-Poincaré characteristic are set functions that describe the geometric and topological structure of a *regular* set pretty well; cf. e.g. [1]. Known in integral and convex geometry also as *intrinsic volumes* or *quermaßintegrals* and in physics and differential geometry as *curvature measures*, these functionals are used in morphological image analysis for the characterization of binary and gray-scale images. They are successfully applied to various problems in astronomy, materials science, medicine, and biology; cf. [2], [3], [4], [5], [6], [7], [8].

Beginning with the pioneering work of Serra [9], several approaches to the computation of single Minkowski functionals such as the Euler number have been proposed e.g. in [5], [10], and [11]. In recent papers [12], [13] and [14], alternative methods are proposed allowing for the simultaneous computation of all Minkowski functionals of sets from different regularity classes such as *polyconvex sets* or *sets with positive reach*. The above methods can be modified to estimate the specific intrinsic volumes of stationary random closed sets by introducing an appropriate edge correction. In this case, it is assumed that the given data is part of a realization of an unbounded spatially homogeneous random closed set observed within a bounded sampling window. Alongside with the development of theoretical methods, the algorithmic issues of the computation of Minkowski functionals of discrete sets given on lattices or *binary images* have been touched upon in [5], [15], [16], [17], [18], and [19].

In the present paper, we embed the methods proposed in [12] and [13] in the general context provided by the theorem of Hadwiger and the method of moments; see Sections 2.2 and 3.2 for details. Furthermore, we discuss the corresponding algorithms for these methods in Section 2.4 and give their edge–corrected counterparts for the estimation of specific intrinsic volumes of random sets in Section 3.3. A comparison of the numerical results with those of methods from [5] and [19] is provided in Sections 2.5 and 3.5. The paper concludes with a brief discussion of numerical results in Section 4.

In the theoretical part of the paper (Sections 2.1–2.2 and 3.1–3.2), binary images of arbitrary dimension $d \geqslant 2$ are considered. In this way, we emphasize that the proposed computational methods are independent of d. However, the implementation clearly depends on the dimension. This is the reason why we give the algorithms and numerical results in dimension $d = 2$ only. The implementation of the algorithms in three dimensions and the corresponding numerical studies are ongoing research. They will be considered in a forthcoming paper.

The proposed algorithms seem to be relatively complex in comparison with

other known methods. As a consequence, they are slower than e.g. the very efficient algorithms given in [9]. This is the price one has to pay for the nice statistical properties of these methods that allow their use in image comparison based on asymptotical Gauss tests (see [20] for details).

2 Computation of intrinsic volumes for deterministic sets

In this section, we discuss methods for the computation of Minkowski functionals for deterministic sets. For the sake of convenience, we rather use *intrinsic volumes* which differ from Minkowski functionals by a constant factor and by the inverse order of notation; cf. [21]. First, preliminaries on intrinsic volumes are given. Then, computational methods based on Hadwiger's expansion are described for arbitrary dimensions d. In Section 2.3, binary images are introduced as discretizations of polyconvex sets in $\mathbb{R}^2$. An algorithm for the computation of intrinsic volumes of binary images is given in Section 2.4. Finally, numerical results are discussed.

2.1 Intrinsic volumes of polyconvex sets

Let $\mathcal{K}$ be the set of all compact convex subsets of $\mathbb{R}^d$. A set is called *polyconvex* if it is a finite union of sets from $\mathcal{K}$. The class $\mathcal{R}$ of all polyconvex sets in $\mathbb{R}^d$ is often called the *convex ring*. This set family is general enough to model most objects in image analysis in the sense of approximation of these objects by unions of polyhedra as explained in Section 2.3 for the two–dimensional case. Let $A \oplus B = \{x + y : x \in A,\ y \in B\}$ be the *Minkowski sum* of sets A and B. Denote by $B_r(x)$ the ball of radius $r > 0$ centered in $x \in \mathbb{R}^d$. For any set $K \subset \mathbb{R}^d$, the set of inner points of K in $\mathbb{R}^d$ is denoted by $\mathrm{int}(K) = K \setminus \partial K$, where ∂K is the boundary of K.

For a set $K \in \mathcal{K}$, the *intrinsic volumes* $V_0(K), \ldots, V_d(K)$ are usually introduced as coefficients in the polynomial expansion of the volume (or Lebesgue measure) $V_d(K \oplus B_r(o))$ of the *parallel neighborhood* $K \oplus B_r(o)$ of K with respect to r:

$$V_d(K \oplus B_r(o)) = \sum_{j=0}^{d} r^{d-j} \kappa_{d-j} V_j(K)\,, \tag{1}$$

where $\kappa_j = V_j(B_1(o))$ is the j–volume of the j–dimensional unit ball. By additivity, V_j can be extended in a unique way to $\mathcal{R}$, namely,

$$V_j(K_1 \cup \ldots \cup K_n) = \sum_{i=1}^{n} (-1)^{i-1} \sum_{1 \leqslant j_1 < \ldots < j_i \leqslant n} V_j(K_{j_1} \cap \ldots \cap K_{j_i}) \tag{2}$$

for any $K_1, \dots, K_n \in \mathcal{K}$ and $j = 0, \dots, d$. It can be shown that for any $K \in \mathcal{R}$ $2V_{d-1}(K)$ is the surface area and $V_0(K)$ is the Euler–Poincaré characteristic, that is, a linear combination of *Betti numbers* of K; see e.g. [1] and [11]. In two dimensions, $V_0(K)$ is equal to the number of "clumps" minus the number of "holes" in $K \in \mathcal{R}$. For compact sets K with C^2–smooth boundary ∂K, intrinsic volumes $V_j(K)$ are integrals of mean curvature of ∂K, cf. [1].

Formula (1) is often referred to as the *Steiner formula*. It is a special case of the well–known result of Hadwiger (cf. [22]): any additive rigid motion invariant continuous functional F on $\mathcal{R}$ can be represented as a linear combination of intrinsic volumes, i.e.,

$$F(K) = \sum_{j=0}^{d} a_j V_j(K), \quad K \in \mathcal{R} \tag{3}$$

with coefficients $a_0, \dots, a_d \in \mathbb{R}$. These coefficients can be defined from the following system of linear equations

$$F(K_i) = \sum_{j=0}^{d} a_j V_j(K_i), \quad i = 0, \dots, d, \tag{4}$$

where $K_0, \dots, K_d$ are simple convex bodies (for instance, a ball, a segment, a square, a cube, and so on) for which the values of F and of V_j can easily be computed and the matrix $(V_j(K_i))$ in (4) is not singular.

2.2 Computation of intrinsic volumes

Suppose that there exist functionals $F_0, \dots, F_n$, $n \geqslant d$ on $\mathcal{R}$ satisfying the assumptions of the characterization theorem of Hadwiger with coefficients a_{ij} from the expansion

$$F_i(K) = \sum_{j=0}^{d} a_{ij} V_j(K), \quad i = 0, \dots, n, \quad K \in \mathcal{R} \tag{5}$$

that are either known or can be assessed by method (4). If $n = d$ and the matrix $A = (a_{ij})$ is regular then the vector $V(K) = (V_0(K), \dots, V_d(K))^\top$ of intrinsic volumes of any polyconvex set K is the solution of the system of equations (5). In the matrix form, it holds $V(K) = A^{-1}F(K)$, where $F(K) = (F_0(K), \dots, F_d(K))^\top$. For the reasons of computational stability, it is more convenient to consider $n \gg d$ and solve the overdetermined system of linear equations (5) by means of the least–squares method. Namely, the unique solution $V^*(K) = (A^\top A)^{-1} A^\top F(K)$ of the minimization problem

$$\Big| F(K) - A\,V^*(K) \Big| = \min_{x \in \mathbb{R}^d} \Big| F(K) - A\,x \Big| \tag{6}$$

is a good approximation of $V(K)$. Notice that the values $V_d^*(K)$ and $V_{d-1}^*(K)$ have to be non–negative since they approximate the volume and half the surface area of K. If the matrix $A^\top A$ is almost singular one might try to change the set of functionals F_i in order to get $det(A^\top A) \gg 0$. For functionals given in (7) and (11) this can be done by changing the values of radii r_i. Alternatively, the singular value decomposition can be used.

Examples for functionals F_i, $i = 0, \ldots, n$ given in [12] and [13] are based on the explicit extension of the Steiner formula to the convex ring and the principal kinematic formula. In the first case, the value $F_i(K)$, $K \in \mathcal{R}$ is given by the volume $\rho_{r_i}(K)$ of $\left(K \oplus B_{r_i}(o)\right) \setminus K$ counted "with multiplicity":

$$\rho_{r_i}(K) = \int\limits_{\partial K \oplus B_{r_i}(o)} \sum_{q \in \partial K,\, q \neq x} J\left(K \cap B_{r_i}(x), q, x\right)\, dx, \tag{7}$$

where $J\left(B, q, x\right)$ is the *index* of $B \in \mathcal{R}$ defined by

$$J(B, q, x) = \left(1 - \lim_{\delta \to +0} \lim_{\varepsilon \to +0} V_0\left(B \cap B_{|x-q|-\varepsilon}(x) \cap B_\delta(q)\right)\right) \mathbf{1}_{\partial B}(q)$$

for any $q, x \in \mathbb{R}^d$, $q \neq x$. Here $\mathbf{1}_{\partial B}(\cdot)$ is the usual indicator function of the set ∂B. The value of $J(B, q, x)$ can be interpreted as the "local connectivity" of B at the boundary point q regarded from the point x. If B is convex then the index of B is zero for all $x \in B$ and one for $x \notin B$ such that q is the metrical projection of x onto ∂B. For polyconvex sets B, a similar interpretation is possible by the additivity of the index. In two dimensions, each point x of the volume (7) is weighted by the number of its metric projections onto ∂K minus the number of *concavity* points of the boundary ∂K lying within the distance r_i from x; cf. [23] for details. Radii $r_0, \ldots, r_n$ have to be positive and pairwise different. The matrix A determined by the *generalized Steiner formula*

$$\rho_{r_i}(K) = \sum_{j=0}^{d-1} r^{d-j} \kappa_{d-j} V_j(K), \quad K \in \mathcal{R} \tag{8}$$

is equal to

$$A = \begin{pmatrix} r_0^d\kappa_d & r_0^{d-1}\kappa_{d-1} & \ldots & r_0^2\kappa_2 & r_0\kappa_1 & 0 \\ r_1^d\kappa_d & r_1^{d-1}\kappa_{d-1} & \ldots & r_1^2\kappa_2 & r_1\kappa_1 & 0 \\ \ldots & \ldots & \ldots & \ldots & \ldots & \ldots \\ r_n^d\kappa_d & r_n^{d-1}\kappa_{d-1} & \ldots & r_n^2\kappa_2 & r_n\kappa_1 & 0 \end{pmatrix}. \tag{9}$$

Since the last column in the above matrix is zero, it is useful to omit this column and to exclude the variables x_d and $V_d(K)$ from consideration in the equation (6).

In the second case, the principal kinematic formula yields

$$\int\limits_{K\oplus B_{r_i}(o)} V_0(K\cap B_{r_i}(x))\,dx = \sum_{j=0}^{d} r^{d-j}\kappa_{d-j}V_j(K)\,, \quad K\in\mathcal{R}. \tag{10}$$

If we set

$$F_i(K) = R_{r_i}(K) = \int\limits_{K\oplus B_{r_i}(o)} V_0(K\cap B_{r_i}(x))\,dx \tag{11}$$

for any pairwise different $r_i > 0$, $i = 0,\dots,n$, the matrix A looks like

$$A = \begin{pmatrix} r_0^d\kappa_d & r_0^{d-1}\kappa_{d-1} & \dots & r_0^2\kappa_2 & r_0\kappa_1 & 1 \\ r_1^d\kappa_d & r_1^{d-1}\kappa_{d-1} & \dots & r_1^2\kappa_2 & r_1\kappa_1 & 1 \\ \dots & \dots & \dots & \dots & \dots & \dots \\ r_n^d\kappa_d & r_n^{d-1}\kappa_{d-1} & \dots & r_n^2\kappa_2 & r_n\kappa_1 & 1 \end{pmatrix}. \tag{12}$$

As it is seen from the comparison of matrices in (9) and (12), functionals $\rho_{r_i}(K)$ and $R_{r_i}(K)$ are related to each other by the identity $R_{r_i}(K) = \rho_{r_i}(K)+V_d(K)$ for any $K\in\mathcal{R}$. This also explains the fact that the volume of K cannot be determined by the method based on the Steiner formula. However, both methods lead to completely different numerical algorithms; see [13], [18], and Section 2.4 for details.

A much more general class of functionals F_i and matrices A can be constructed by means of the *generalized principal kinematic formula* given e.g. in [21], p. 253.

2.3 Discretized sets and polygonal approximation

Consider an arbitrary polyconvex set $K\subset\mathbb{R}^2$. In computer applications one often deals with binary images. We assume that the *discretization* $K\cap\mathbb{L}^2$ of K with respect to the quadratic *lattice* $\mathbb{L}^2 = \Delta\mathbb{Z}^2 + l_0$ with the *lattice spacing* $\Delta > 0$ and the *offset* $l_0 = (l_{0,x}, l_{0,y})^\top \in \mathbb{R}^2$ is given. Moreover, any extra information about K is not available. It is convenient to interpret $K\cap\mathbb{L}^2$ as a binary image, i.e., as a finite set of "black" or foreground pixels $x\in K\cap\mathbb{L}^2$ on the "white" grid $\mathbb{L}^2$ (the so–called background). This means that we identify the set $K\cap\mathbb{L}^2$ with its indicator function $\mathbf{1}_{K\cap\mathbb{L}^2}:\mathbb{L}^2\to\{0,1\}$, i.e., $\mathbf{1}_{K\cap\mathbb{L}^2}(x) = 1$ if $x\in K\cap\mathbb{L}^2$, and $\mathbf{1}_{K\cap\mathbb{L}^2}(x) = 0$, otherwise. Since K is bounded, the binary image is often represented as a matrix $B = (b_{i,j})_{0\leqslant i<n_y, 0\leqslant j<n_x}$ with $b_{i,j} = \mathbf{1}_{K\cap\mathbb{L}^2}((j\Delta+l_{0,x}, i\Delta+l_{0,y}))$ for $0\leqslant i<n_y$, $0\leqslant j<n_x$. To avoid problems with 2×2 pixel configurations at the boundary of $K\cap\mathbb{L}^2$, we assume w. l. g.

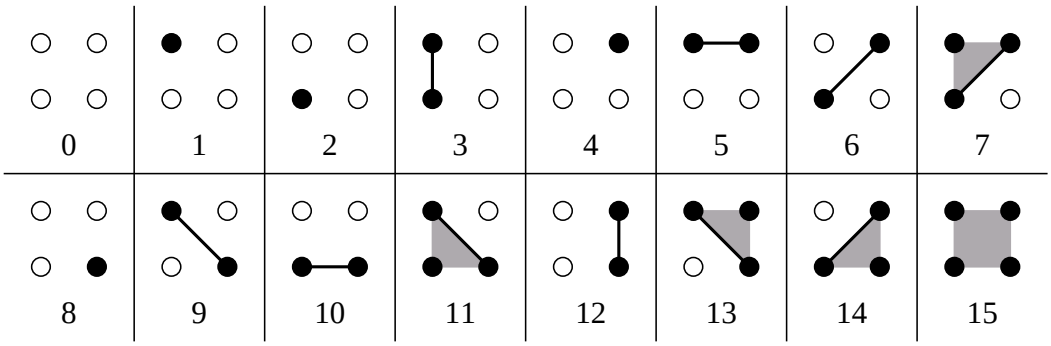

Fig. 1. All 2×2 neighborhood configurations in two dimensions together with possible codes and polygonal approximations.

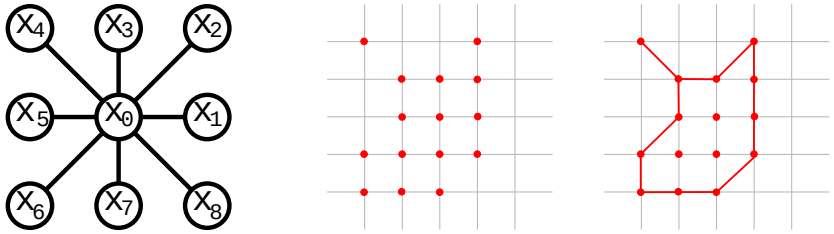

(a) (b)

Fig. 2. (a) 8–neighborhood relation and (b) approximation of a discretized set by $\mathbb{F}$.

that all boundary pixels of the image are white, that is, $b_{i,j} = 0$ for $i = 0$, $i = n_y - 1$, $j = 0$, and $j = n_x - 1$.

Neighborhood configurations are possible configurations of neighboring pixels. For two–dimensional binary images, commonly 2×2 neighborhood configurations are used, i. e. 4–tuples of neighboring pixels $(b_{i,j}, b_{i+1,j}, b_{i,j+1}, b_{i+1,j+1})$. Of course, configurations of other size are also imaginable. Figure 1 shows all 16 possible 2×2 neighborhood configurations in two dimensions. For each configuration, possible polygonal approximations with vertices belonging to the grid $\mathbb{L}^2$ and the associated boundary are depicted. This approximation is based on the *8-neighborhood relation* (cf. Figure 2 (a)).

Each neighborhood configuration can be assigned a code, for example $c_{i,j} = b_{i,j} \cdot 2^0 + b_{i+1,j} \cdot 2^1 + b_{i,j+1} \cdot 2^2 + b_{i+1,j+1} \cdot 2^3$. In this case, each of these 16 configurations is associated with a unique number between 0 and 15 (cf. Figure 1). The absolute frequency of a configuration with code k within the binary image B can be given as $h_k = \sum_{i=0}^{n_y-2} \sum_{j=0}^{n_x-2} \delta_k(c_{i,j})$ for $k = 0, \ldots, 15$, where $\delta_\cdot(\cdot)$ denotes the Kronecker delta. The vector h of absolute frequencies $h = (h_0, \ldots, h_{15})$ is called the *neighborhood histogram*. See [9], [5] for more details and for the efficient computation of h.

To compute the left–hand side (7) and (11) of the system of linear equations (5) for a set $K \in \mathcal{R}$ from its discretization $K \cap \mathbb{L}^2$, one has to define the "boundary"

of $K \cap \mathbb{L}^2$. In other words, the boundary of K has to be "reconstructed" from its discretized version $K \cap \mathbb{L}^2$. One possible way to do that is to approximate K by a union of polygons with vertices belonging to the grid $\mathbb{L}^2$. To describe this approximation procedure more formally, an *approximation system* $\mathbb{F}$ can be used which consists of all vertices, edges, triangles, and squares of the whole $\mathbb{L}^2$ as depicted in Figure 1. The "construction bricks" $K \sqcap \mathbb{F}$ for the approximation of K with respect to $\mathbb{F}$ contain all elements of $\mathbb{F}$ whose vertices lie in $K \cap \mathbb{L}^2$. Therefore, the *polygonal approximation* $K_{\mathbb{F}}$ of K with respect to $\mathbb{F}$ can be defined as $K_{\mathbb{F}} = \bigcup_{P \in K \sqcap \mathbb{F}} P$. The above approximation procedure implicitly uses the notion of connectivity on graphs as considered in [9].

A point $x \in K \cap \mathbb{L}^2$ is called a *boundary point* with respect to the system $\mathbb{F}$ if $x \in \partial K_{\mathbb{F}}$. The boundary $\partial K_{\mathbb{F}}$ obtained by the polygonal approximation shown in Figure 1 could be described by *Freeman's chain code* with 8 directions; cf. [24]. The set of all boundary points of $K \cap \mathbb{L}^2$ is denoted by $\partial(K \cap \mathbb{L}^2)$. In other words, a foreground pixel x_0 belongs to $\partial(K \cap \mathbb{L}^2)$ if there is at least one background pixel in its 4–neighborhood, which consists of x_1, x_3, x_5, and x_7 (cf. Figure 2 (a)).

Figure 2 (b) shows a discretized set $K \cap \mathbb{L}^2$ and its approximation $K_{\mathbb{F}}$. The geometry of the boundary $\partial K_{\mathbb{F}}$ heavily depends on the system $\mathbb{F}$ and on the resolution $1/\Delta$. In particular, significant changes can happen to the connectivity of $K_{\mathbb{F}}$ in comparison to K. Hence, any computation of intrinsic volumes of K based on the discretization $K \cap \mathbb{L}^2$ and approximation $K_{\mathbb{F}}$ is subject to a substantial error. This phenomenon is well–known especially in the case of the Euler–Poincaré characteristic; see e.g. [9], p. 220.

2.4 Algorithms

In the sequel, an algorithm for the computation of intrinsic volumes based on the principal kinematic formula (see formulae (11), (12)) is given in two dimensions. Generalizations to the d–dimensional case are straightforward. The algorithm based on the Steiner formula is described in detail in [18].

The computation of intrinsic volumes $V(K)$ of any set $K \in \mathcal{R}$ is reduced to the computation of integrals in (11) and subsequent solving the least squares problem (6) for the polygonal approximation $K_{\mathbb{F}}$ of K. The integrals $R_{r_i}(K)$ can be approximated by

$$\widehat{R}_{r_i}(K_{\mathbb{F}}) = \widetilde{\Delta}^2 \sum_{k=1}^{m} V_0\Big(\big(K \cap B_{r_i}(x_k)\big)_{\mathbb{F}}\Big), \tag{13}$$

where the points $x_1, \ldots, x_m$ belong to a two–dimensional quadratic lattice with mesh size $\widetilde{\Delta} \geqslant \Delta$. Here, the set $K \cap B_{r_i}(x_k)$ is discretized with respect to

the lattice $\mathbb{L}^2$ where $B_{r_i}(x_k)$ is the ball with center x_k and radius r_i in $\mathbb{R}^2$ with respect to the Euclidean distance. Thus, the vector $V(K)$ can be computed numerically as

$$V(K) \approx \left(A^\top A\right)^{-1} A^\top \widehat{R}(K_\mathbb{F})\,, \tag{14}$$

where $\widehat{R}(K_\mathbb{F}) = (\widehat{R}_{r_0}(K_\mathbb{F}), \ldots, \widehat{R}_{r_n}(K_\mathbb{F}))^\top$.

The Euler number

$$V_0\Big(\big(K \cap B_{r_i}(x_k)\big)_\mathbb{F}\Big) \tag{15}$$

can be computed by an arbitrary method known in the literature. We use the simplest way based on the inclusion-exclusion formula (2). Namely, the set $(K \cap B_{r_i}(x_k))_\mathbb{F}$ is a union of elementary convex polygons from $\mathbb{F}$. These can be points, segments, triangles, or squares with vertices on the lattice $\mathbb{L}^2$. Formula (2) applies directly to their union. This computation is easy to convey since the Euler number of any compact convex set is either zero in case it is empty or one, otherwise.

To perform the computation of (13) efficiently, we have to avoid multiple scans of the image B, which is the matrix representation of $K \cap \mathbb{L}^2$. Naively, one scan of the image would be necessary for each point x_k and each radius r_i, $k = 1, \ldots, m$; $i = 1, \ldots, n$. However, it can be improved in such a way that only one scan is required to compute (15) for all radii r_i at a point x_k. To this end, we compute the frequencies $h_k[i][l]$ of the configurations with codes $l = 0, \ldots, 15$ of the image $K \cap B_{r_i}(x_k)$ for all $k = 1, \ldots, m$ and $i = 0, \ldots, n$. In other words, for each point x_k and each radius r_i the neighborhood histogram $h_k[i]$ of the image $K \cap B_{r_i}(x_k)$ must be calculated. The basic idea is as follows. Let the radii form an arithmetical progression $r_i = r_0 + i\Delta_r$ for some $r_0 > 0$ and $\Delta_r > 0$. We use the data structure of [25] and apply it to the counting of pixel configurations. This is combined with the Euclidean distance transform, which can easily be computed for an image that contains exactly one "white" pixel (namely x_k) and is "black" besides this. Furthermore, the pixels of a configuration are ordered with increasing distance to x_k using the idea of Voronoi diagrams.

In the following, we concentrate on the computation of $V_0((K \cap B_{r_i}(x_k))_\mathbb{F})$ for one point x_k and all radii r_i. First we determine the contribution of a single configuration (p_0, p_1, p_2, p_3) as shown in Figure 3 (a) to the neighborhood histogram $(h_k[i][0], \ldots, h_k[i][15])$ for all radii r_i. A pixel p_l, $l = 0, \ldots, 3$ from the configuration is "black" in the discretization of $K \cap B_{r_i}(x_k)$ if it is "black" in the discretization of K and if its (Euclidean) distance to x_k is at most r_i. Therefore, each "white" pixel of $K \cap \mathbb{L}^2$ is also "white" within $K \cap \mathbb{L}^2 \cap B_{r_i}(x_k)$. If the distance between the pixel and x_k is less than or equal to r_j and greater than r_{j-1} $(0 \leqslant j \leqslant n)$ then each "black" pixel of $K \cap \mathbb{L}^2$ is "white" within $K \cap \mathbb{L}^2 \cap B_{r_i}(x_k)$ for $i < j$ and "black" for $j \leqslant i \leqslant n$. So, each pixel p with $r_{j-1} < |p - x_k| \leqslant r_j$ changes its value only during the transfer from $(K \cap B_{r_{j-1}}(x_k))_\mathbb{F}$

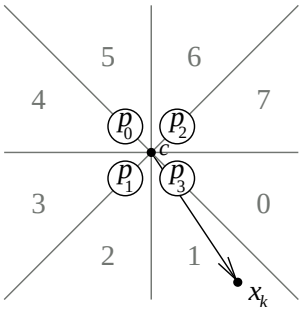

(a)

	region index							
	0	1	2	3	4	5	6	7
0	p_3	p_3	p_1	p_1	p_0	p_0	p_2	p_2
1	p_2	p_1	p_3	p_0	p_1	p_2	p_0	p_3
2	p_1	p_2	p_0	p_3	p_2	p_1	p_3	p_0
3	p_0	p_0	p_2	p_2	p_3	p_3	p_1	p_1

(b)

Fig. 3. Sorting the pixels of a neighborhood configuration (p_0, p_1, p_2, p_3) with increasing distance to x_k based on the region x_k belongs to.

to $(K \cap B_{r_j}(x_k))_{\mathbb{F}}$. Consequently, a neighborhood configuration consisting of four pixels can change its code at most four times within $(K \cap B_{r_{i_l}}(x_k))_{\mathbb{F}}$ for $l = 0, \ldots, 3$. To determine the order in which these changes of the code of the configuration (p_0, p_1, p_2, p_3) occur, the pixels of the configuration have to be sorted according to their distance to x_k. This can be accomplished using the idea of Voronoi diagrams; see [26]. Figure 3 (a) contains all possible edges of Voronoi diagrams induced by the pixels $p_0, \ldots, p_3$ or subsets thereof. These edges determine eight regions $0, 1, \ldots, 7$. For all x_k within one such region, the order of the pixels of the configuration (p_0, p_1, p_2, p_3) is the same with respect to their distance to x_k. Therefore, the angle of the vector $x_k - c$ starting at the center of gravity c of $p_0, \ldots, p_3$ and ending at x_k has to be determined and translated into the index of the regions $0, 1, \ldots,$ and 7 shown in Figure 3 (a). Using the region index as a column index in the table of Figure 3 (b) yields the sorted sequence of pixels with increasing distance to x_k in rows $0, \ldots, 3$ of the respective column.

Let $s[q][t]$ denote the index of the pixel in the q-th row and t-th column of the table in Figure 3 (b). Each configuration (p_0, p_1, p_2, p_3) has to be counted for all radii r_i. However, the code of this configuration may change as said above at most four times. Let $r_{i_0}, r_{i_1}, \ldots, r_{i_3}$ be the radii which produce the change of the configuration code. These radii can be determined through the distance of the pixels in sorted order, i. e. $i_l = \lceil (d_{s[l][t]} - r_0)/\Delta_r \rceil$, $l = 0, \ldots, 3$, where d_q denotes the distance from p_q to x_k and j is the index of the region x_k belongs to.

After having processed all configurations, $V_0((K \cap B_{r_i}(x_k))_{\mathbb{F}})$ can easily be computed from the neighborhood histogram $(h_k[i][0], \ldots, h_k[i][15])$ and the inclusion-exclusion formula. In the following, the algorithm is described in more detail:

1 Initialize $h_k[i][l] := 0$ for each $i = 0, \ldots, n$ and $l = 0, \ldots, 15$.
2 For each neighborhood configuration (p_0, p_1, p_2, p_3) of the binary image with c being the center of gravity of p_0, p_1, p_2, and p_3 do

2.1 Let d_0, d_1, d_2, d_3 be the distances of $p_0, \ldots, p_3$ to x_k, respectively.
2.2 Compute the index t of the region that contains x_k using the angle of the vector $x_k - c$ as depicted in Figure 3 (a).
2.3 Using the table in Figure 3 (b), $s[q][t]$ yields the index of the q-th pixel in sorted order for $q = 0, \ldots, 3$.
2.4 Initialize $konf := 0$.
2.5 $h_k[0][konf] := h_k[0][konf] + 1$
2.6 For $q = 0, \ldots, 3$ do: If the pixel $p_{s[q][t]}$ is black then
2.6.1 Compute $di := \lceil (d_{s[q][t]} - r_0)/\Delta_r \rceil$.
2.6.2 If $di > n$ then go to step 2.
2.6.3 Else if $di \geqslant 0$ then
$h_k[di][konf] := h_k[di][konf] - 1$
$konf := konf + 2^{s[q][t]}$
$h_k[di][konf] := h_k[di][konf] + 1$

3 For $l = 0, \ldots, 15$ do
For $i = 1, \ldots, n$ do
$h_k[i][l] := h_k[i][l] + h_k[i-1][l]$

4 Compute $V_0((K \cap B_{r_i}(x_k))_{\mathbb{F}})$ from the neighborhood histogram $(h_k[i][0], \ldots, h_k[i][15])$ using the inclusion-exclusion formula (or any other method) for $i = 0, \ldots, n$

The above algorithm must be repeated for each x_k, $k = 1, \ldots, m$. The total run-time of the presented algorithm is $O(mN)$, where $N = n_x n_y$ is the size of the binary image, i. e. the number of its pixels, since the computation of $V_0(\cdot)$ can be done in time proportional to the size of the neighborhood histogram. Usually, the number m of sampling points x_k is much smaller than the size of the image N, i. e. $m \ll N$.

Numerical solution (14) heavily depends on the choice of the radii $r_0, \ldots, r_n$. Moreover, it does not necessarily preserve the positivity property of the area $V_2(K)$ and the boundary length $2V_1(K)$. The following radii can be practically recommended for use on the basis of our empirical studies: $r_0 = 4.2$, $r_{i+1} = r_i + 1.3$, $0 \leqslant i < 15$. With these radii, V_1 is computed with an acceptable precision, but the accuracy of computation of V_0 varies in dependence of the input image. Our experiments showed that increasing the computational precision for V_1 leads to a decrease in the precision of V_0, and vice versa. Unfortunately, there seems to be no choice of radii to compute both V_0 and V_1 with the same precision for any input image.

2.5 Numerical results

To compare the algorithms given in Section 2.4 and papers [18] and [19], the results for two images given in Figure 4 are presented. The reference values

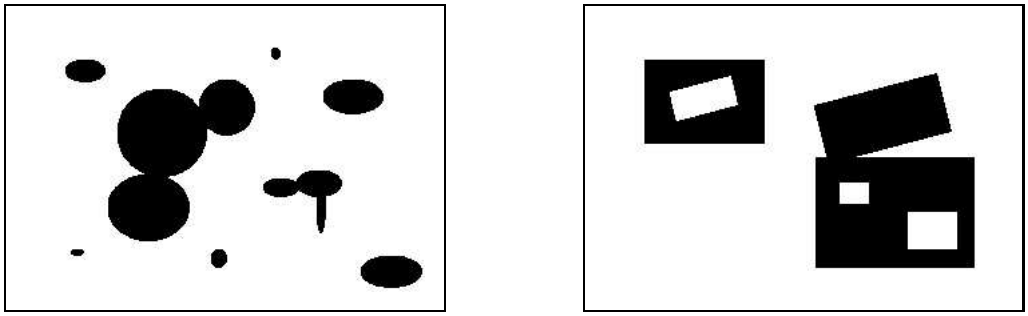

(a) (b)

Fig. 4. Test binary images.

Table 1
Overview of the methods used in Tables 2–3

Method	based on
(i)	inclusion–exclusion formula (2)
(ii)	paper [19] by Mrkvička and Rataj
(iii)	Steiner formula; see paper [18]
(iv)	principal kinematic formula; see Section 2.4

Table 2
Computation results for image (a) of Figure 4

Algorithm	$V_2(K)$	δ	$2V_1(K)$	δ	$V_0(K)$	δ
(i)	10391.50	—	1063.62	—	8.00	—
(ii)	—	—	1073.98	0.97%	4.09	-48.88%
(iii)	—	—	1060.74	-0.27%	8.00	0.00%
(iv)	10464.64	0.70%	1013.31	-4.73%	7.27	-9.13%

Table 3
Computation results for image (b) of Figure 4

Algorithm	$V_2(K)$	δ	$2V_1(K)$	δ	$V_0(K)$	δ
(i)	16725.50	—	1310.98	—	-1.00	—
(ii)	—	—	1033.03	-21%	-1.72	72%
(iii)	—	—	1310.80	-0.01%	-1.00	0.00%
(iv)	16461.02	-1.58%	1295.23	-1.20%	-0.94	-6.22%

of the Minkowski functionals for these images are obtained by the application of the inclusion-exclusion formula (2) which computes these values exactly on the basis of the polygonal approximation of Section 2.3.

The results for the images (a) and (b) of Figure 4 are shown in Tables 2 and

3, respectively. In these tables, δ stands for the relative error (in percent) of the computation results with respect to the corresponding value obtained by the inclusion-exclusion formula. Note that $V_2(K)$ cannot be computed by methods (ii) and (iii). Both images were analyzed using the same parameters $\widetilde{\Delta} = 5$, $r_0 = 4.2$, $r_{i+1} = r_i + 1.3$ for $0 \leqslant i < 12$ in the method (iv). It can be seen from Tables 2 and 3 that methods (ii) and (iv) yield biased results. The bias of the area computed by method (iv) is quite surprising. It can be diminished by better choice of radii r_i. At the same time, this can lead to worse results for the boundary length and Euler number as pointed out at the end of Section 2.4. On the contrary, the algorithm (iii) is precise and hence can be preferred for the analysis of deterministic images. Another reason for the choice of this algorithm is its complexity $O(N)$ where N is the number of pixels in the image. This leads to a run–time of 0.9 sec. per image (Pentium IV, 2.8 GHz, $N = 60000$). For comparison, the corresponding run–time of method (iv) is 4 sec. per image.

3 Computation of specific intrinsic volumes for stationary random closed sets

Suppose that the analysed binary image is a realization of a certain stochastic model observed within a sampling window $W \in \mathcal{K}$. A reasonable class of such models is provided by *random closed sets* (RaCS) with realizations from the *extended convex ring* briefly introduced in Section 3.1. Their intrinsic volumes averaged over all realizations and increasing observation windows are called *specific intrinsic volumes*. A modification of the method of moments for the estimation of specific intrinsic volumes from one single binary image is given in Section 3.2. Corresponding algorithmic issues and numerical results are discussed in Sections 3.3 and 3.5.

3.1 Stationary random closed sets

Let Ξ be a random closed set in $\mathbb{R}^d$, i.e., Ξ can be considered as a random element whose values are closed sets. Simple examples for RaCS are random points or closed spheres of random midpoints and random radii. The realizations ξ of Ξ are taken from the extended convex ring $\mathcal{S}$, i.e., $\xi \cap K$ belongs to the usual convex ring $\mathcal{R}$ for any $K \in \mathcal{K}$ and almost every realization ξ of Ξ. See e.g. [27] and [26] for the exact definition and properties of RaCS. The random closed set Ξ is *stationary* if its probability distribution is translation invariant.

For any nonempty $K \in \mathcal{R}$, let $N(K) = \min\{m \in \mathbb{N} : K = \bigcup_{i=1}^m K_i, K_i \in \mathcal{K}\}$

be the minimal number of convex components of the polyconvex set K, where we put $N(K) = 0$ if $K = \emptyset$. If $E\, 2^{N(\Xi \cap [0,1]^d)} < \infty$, then for any monotonously increasing sequence of compact and convex observation windows $W_k = k\, K_0$, $K_0 \in \mathcal{K}$ such that $V_d(K_0) > 0$ and $o \in \mathrm{int}(K_0)$, the expectations $E\, V_j(\Xi \cap W_k)$ are well defined. Moreover, for each $j = 0, \ldots, d$, the limit

$$\overline{V}_j(\Xi) = \lim_{k \to \infty} \frac{E\, V_j(\Xi \cap W_k)}{V_d(W_k)} \tag{16}$$

exists and is called the j-th *specific intrinsic volume* of Ξ.

3.2 Estimation of specific intrinsic volumes

Suppose that there exist random fields $Y_i = \{Y_i(x),\ x \in \mathbb{R}^d\}$, $i = 0, \ldots, n$, $n \geqslant d$ such that Y_i are *stationary of second order*. It means that $E\, Y_i(x) = \mu_i$ does not depend on $x \in \mathbb{R}^d$ and the covariance $Cov(Y_i(x), Y_i(x+h)) = Cov_{Y_i}(h)$ depends only on $h \in \mathbb{R}^d$ for all i. Furthermore, we assume that their mean values μ_i can be represented as $\mu_i = \sum\limits_{j=0}^{d} a_{ij} \overline{V}_j(\Xi)$, where the matrix $A = (a_{ij})$ of constant coefficients a_{ij} is regular for $n = d$. Then, it holds

$$\overline{V}(\Xi) = A^{-1} \mu \tag{17}$$

for $n = d$, where $\overline{V}(\Xi) = \left(\overline{V}_0(\Xi), \ldots, \overline{V}_d(\Xi)\right)^\top$ and $\mu = (\mu_0, \ldots, \mu_n)^\top$.

It follows from (17) that random fields Y_i must be somehow connected with the random set Ξ. A sufficiently large family of such fields is given in [20]. There, one puts $Y_i(x) = f_i((\Xi - x) \cap K_i)$ for a conditionally bounded additive set functional f_i and a small scanning window K_i. In what follows, concrete examples of such fields will be given; see also [20]. One can expect that such examples are constructed from set functionals F_i of the form (5). If F_i are given by relation (7) then

$$Y_i(x) = \sum_{q \in \partial\Xi \cap B_{r_i}(x) \setminus \{x\}} J\Big(\Xi \cap B_{r_i}(x), q, x\Big), \quad x \in \mathbb{R}^d \tag{18}$$

and the matrix A from equation (17) is equal to (9). For F_i given by (11), corresponding random fields have the form

$$Y_i(x) = V_0(\Xi \cap B_{r_i}(x)), \quad x \in \mathbb{R}^d \tag{19}$$

for pairwise different positive radii r_i. In this case, matrix A coincides with (12).

If a single realization ξ of Ξ is given in the observation window W, the mean values μ_i of random fields Y_i can be estimated as $\widehat{\mu}_i = \int_W Y_i(x)\, w_i(dx)$, where

$w_i(\cdot)$ is a probability measure with support $U_i \subseteq W$. Frequently used weighting measures $w_i(\cdot)$ have the form $w_i(\cdot) = V_d(\,\cdot\, \cap U_i)/V_d(U_i)$ and $w_i(\cdot) = \sum_{k=1}^{m_i} w_{ik}\delta_{x_{ik}}(\cdot)$ with $x_{i1}, \ldots, x_{im_i} \in U_i$, $w_{i1}, \ldots, w_{im_i} > 0$ and $w_{i1}+\ldots+w_{im_i} = 1$. In the above examples, we set $U_i = W \ominus B_{r_i}(o)$ for $i = 1, \ldots, n$ (minus sampling; see Figure 6). The choice of weights w_{ik} and sampling points x_{ik} will be discussed in the next section.

It is obvious that the vector $\widehat{\mu} = (\widehat{\mu}_0, \ldots, \widehat{\mu}_n)^\top$ is an unbiased estimator for $\mu = (\mu_0, \ldots, \mu_n)^\top$. By the method of moments, $\widehat{V}(\Xi) = A^{-1}\widehat{\mu}$ is an unbiased estimator for $\overline{V}(\Xi)$ in the case $n = d$. If a sequence of monotonously increasing observation windows W_k is used, the above estimator is L_2–consistent and asymptotically normally distributed as $k \to \infty$. This fact is used to construct asymptotic Gaussian tests for the estimated specific intrinsic volumes, see [20]. They enable us to compare the geometrical structure of two homogeneous binary images by detecting significant difference in their estimated specific intrinsic volumes.

Similarly to the deterministic case, $n \gg d$ random fields can be used in the least squares method (6) to make the above estimation more robust with respect to the choice of radii r_i.

We also point out that besides the minus sampling considered above, there are many other types of edge correction, which sometimes lead to unbiased estimators; cf. e.g. the overview [28] and references therein as well as the recent paper [29]. For rectangular observation windows, the following edge correction method is computationally very efficient. Suppose that $W = [-a, a]^d$ for some $a > 0$ and consider the "right upper boundary" $\partial^+ W$ of W, where $\partial^+ W = \Big\{x = (x_1, \ldots, x_d) \in W : \max_{1 \leqslant i \leqslant d} x_i = a\Big\}$. For any $i = 0, \ldots, n$, the estimator

$$\widehat{\mu}_i^{\,+} = \frac{F_i(\Xi \cap W) - F_i(\Xi \cap \partial^+ W)}{V_d(W)} \tag{20}$$

is unbiased for μ_i (see e.g. [30, p. 185], [31]), where F_i is a set functional on $\mathcal{R}$ satisfying the assumptions of Hadwiger's theorem. However, it is still not known whether such estimators possess similar asymptotic properties as the one based on minus sampling.

3.3 Edge–corrected modifications of the algorithms

In the following, modifications of the algorithm given in Section 2.4 and in paper [18] for two-dimensional stationary random closed sets are discussed.

Suppose that a single realization ξ of the two-dimensional stationary RaCS Ξ

is observed within a certain (convex and compact) sampling window $W \subset \mathbb{R}^2$. In many cases, this means that Ξ is sampled at the points of intersection $W \cap \mathbb{L}^2$ of W with a regular square grid $\mathbb{L}^2$. Then, the intersection $\xi \cap W \cap \mathbb{L}^2$ is the only information, which is available about Ξ.

Choose an appropriate sequence of radii $r_0, \dots, r_n$. To compute the least-squares estimator of the three–dimensional vector $\overline{V}(\Xi)$ of specific intrinsic volumes of Ξ using random fields (19), one has to select a regular (deterministic) design $\{x_{i1}, \dots, x_{im_i}\} \subset W \ominus B_{r_i}(o)$ for each radius r_i, $i = 0, \dots, n$, such that the circles $B_{r_i}(x_{ik})$ do not overlap much. Several variants of these *exploratory designs* are described e.g. in Chapter 4 of [32]. Local connectivity numbers $V_0(\xi \cap B_{r_i}(x_{ik}))$ for any $i = 0, \dots, n$ and $k = 1, \dots, m_i$ are computed from $\xi \cap W \cap \mathbb{L}^2$ as described in Section 2.4. We use uniform weights $w_{ik} = 1/m_i$, $k = 1, \dots, m_i$ for the computation of estimators $\widehat{\mu}_i$. Finally, the least squares problem (6) has to be solved to get the estimator $\widehat{V}(\Xi)$.

To keep the estimation variance as small as possible, kriging of the mean and optimal designs can be used to select locations $x_{i1}, \dots, x_{im_i} \subset W \ominus B_{r_i}(o)$ and the weights $w_{i1}, \dots, w_{im_i}$ as recommended in [13]. However, our experiments show that this dramatic increase of the complexity of the estimation method does not yield a significant improvement in the quality of estimation. Hence, we can not recommend it for use.

If we would like to use random fields (18) for the computation of $\widehat{V}(\Xi)$ instead of (19), the following modification of the algorithm given in [18] can be proposed. As in Section 2.3, we replace $K = \xi \cap W$ by its polygonal approximation $K_{\mathbb{F}}$. Due to the particular form of the matrix (9), the area fraction $\overline{V}_2(\Xi) = E\, V_2(\Xi \cap W)/V_2(W)$ has to be estimated separately by

$$\widehat{V}_2(\Xi) = \frac{\operatorname{card}(K \cap \mathbb{L}^2)}{\operatorname{card}(W \cap \mathbb{L}^2)},$$

where $\operatorname{card}(C)$ denotes the cardinality of a finite set C.

To estimate the specific boundary length and the Euler–Poincaré characteristic, consider the vector

$$\left(\frac{\rho_{r_0}(K_{\mathbb{F}})}{\Delta^2 \operatorname{card}((W \ominus B_{r_0}(o)) \cap \mathbb{L}^2)}, \dots, \frac{\rho_{r_n}(K_{\mathbb{F}})}{\Delta^2 \operatorname{card}((W \ominus B_{r_n}(o)) \cap \mathbb{L}^2)} \right), \quad (21)$$

where functionals ρ_{r_i} are given by (7). Discretize the integral in (7) with respect to the lattice $\mathbb{L}^2$ as

$$\rho_r(K_{\mathbb{F}}) \approx \Delta^2 \sum_{x \in (\partial K_{\mathbb{F}} \oplus B_r(o)) \cap (W \ominus B_r(o)) \cap \mathbb{L}^2} \; \sum_{q \in \partial K_{\mathbb{F}} \setminus \{x\}} J(K_{\mathbb{F}} \cap B_r(x), q, x) \quad (22)$$

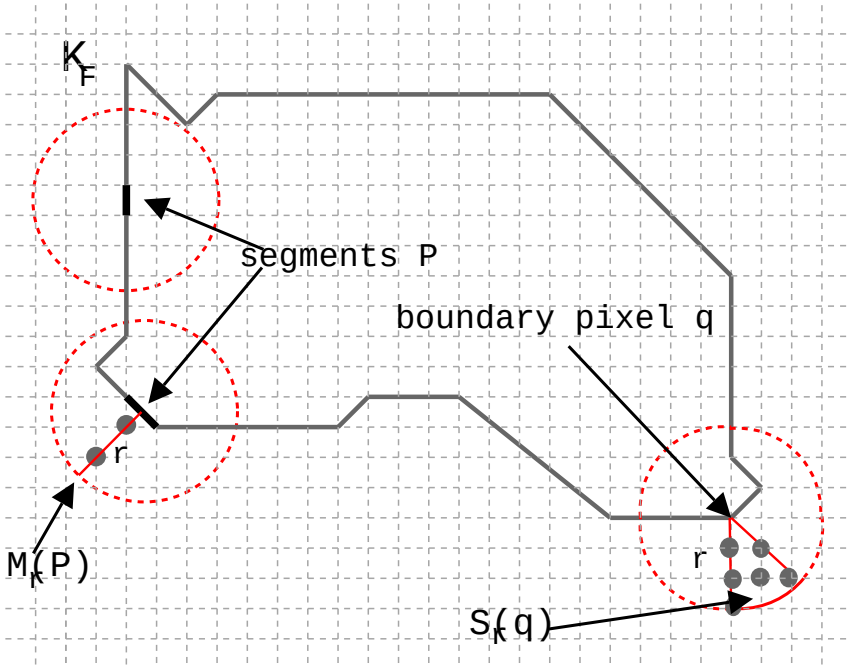

Fig. 5. Computation of $S_r(q)$ and $M_r(P)$

for each $r = r_0, \ldots, r_n$, and, after changing the order of summation, get

$$\rho_r(K_{\mathbb{F}}) \approx \Delta^2 \sum_{q \in \partial(K \cap \mathbb{L}^2)} S_r(q) + \Delta^2 \sum_{P \subset \partial K_{\mathbb{F}}} M_r(P)\,,$$

where

$$S_r(q) = \sum_{x \in (W \ominus B_r(o)) \cap \mathbb{L}^2,\, 0 < |x-q| \leqslant r} J(K_{\mathbb{F}} \cap B_r(x), q, x)$$

and the second sum runs over all diagonal segments with vertices on $\mathbb{L}^2$ of the form 6 and 9 of Figure 1 that belong to the boundary of $K_{\mathbb{F}}$. By $M_r(P)$ we denote the number of all lattice points from $(W \ominus B_r(o)) \cap \mathbb{L}^2$ in the neighborhood $P \oplus B_r(o)$ of a segment P such that they are projected in the interior of P. On Figure 5, $M_r(P)$ is the number of lattice points lying on the outer normal to P at the distance at most r from the diagonal segment P. For any segment P parallel to the grid lines, $M_r(P)$ is evidently equal to zero. The sum $S_r(q)$ is simply the number of lattice points within $B_r(q)$ lying between two outer normals to the boundary of $K_{\mathbb{F}}$. The quantities $S_r(q)$ and $M_r(P)$ depend in general on the location of q and P, respectively. Indeed, only those lattice points x are counted in the above sums which have distance from q (or P, respectively) not larger than r and lie in the reduced sampling window $W \ominus B_r(o)$. However, if the sampling window is large with respect to the radius r, i.e., if $V_2(W \ominus B_{2r}(o)) > 0$, then for lattice points $q \in W \ominus B_{2r}(o)$ and segments $P \subset W \ominus B_{2r}(o)$, the sums $S_r(q)$ and $M_r(P)$ do not depend on the position of q and P and therefore may be computed very fast; see [18] for more details. However, for those q and P being close to the boundary of the window W, the quantities $S_r(q)$ and $M_r(P)$ have to be computed directly

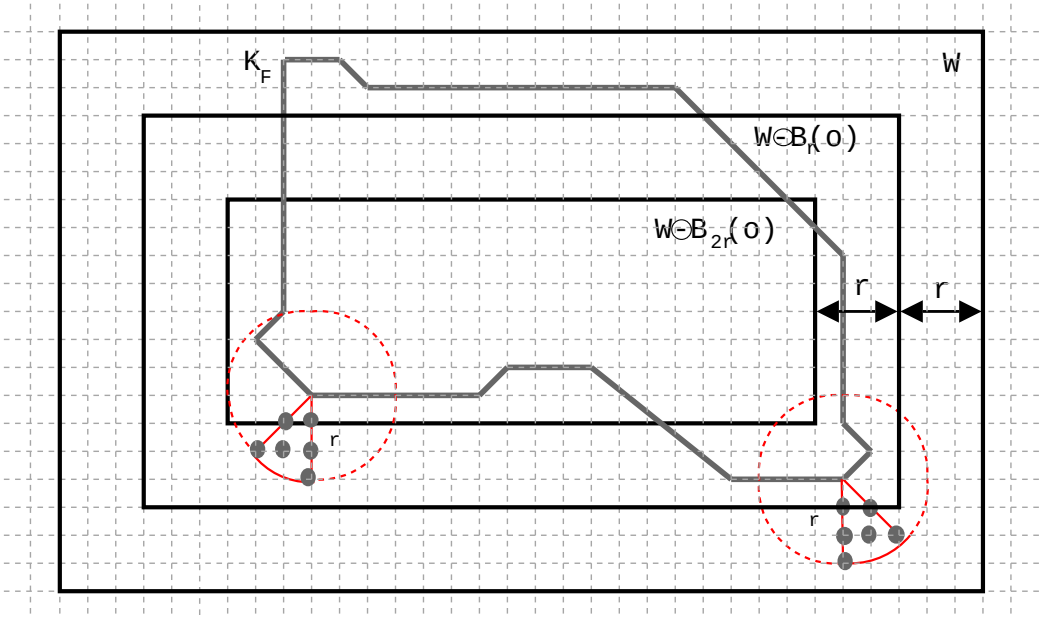

Fig. 6. Minus sampling

which is time consuming; compare Figure 6.

As in [18], this edge–corrected algorithm requires only one single scan of the image. However, the complexity of computation $O(N + lr^2)$ is higher than $O(N)$ in the deterministic case. Here l is the number of boundary points of $K \cap \mathbb{L}^2$ and N the total number of pixels in the image.

For a rectangular observation window W, the edge correction (20) can be used alternatively. Then, the vector (21) must be replaced by

$$\left(\frac{\rho^+_{r_0}(K_{\mathbb{F}}, W)}{\Delta^2 \operatorname{card}(W \cap \mathbb{L}^2)} , \ldots , \frac{\rho^+_{r_n}(K_{\mathbb{F}}, W)}{\Delta^2 \operatorname{card}(W \cap \mathbb{L}^2)} \right) ,$$

where $\rho^+_{r_i}(K_{\mathbb{F}}, W) = \rho_{r_i}(K_{\mathbb{F}} \cap W) - \rho_{r_i}(K_{\mathbb{F}} \cap \partial^+ W)$ for $i = 0, \ldots, n$. Notice that $\rho_{r_i}(K_{\mathbb{F}} \cap W)$ and $\rho_{r_i}(K_{\mathbb{F}} \cap \partial^+ W)$ can be computed in the same way as in the deterministic case. Therefore, this algorithm has complexity $O(N)$.

3.4 Practical choice of dilation radii

Numerical experiments show that the discretization error of the algorithms is smaller for rational r_i than for integer–valued radii. For the method based on the principal kinematic formula, the radii $r_0 = 4.2$, $r_{i+1} = r_i + 1.3$ for $0 \leqslant i < 15$ show an acceptable performance (run–time of 32 sec. per 1000×1000 image, Pentium IV, 2.8 GHz).

For the method based on the Steiner formula and minus sampling, the radii

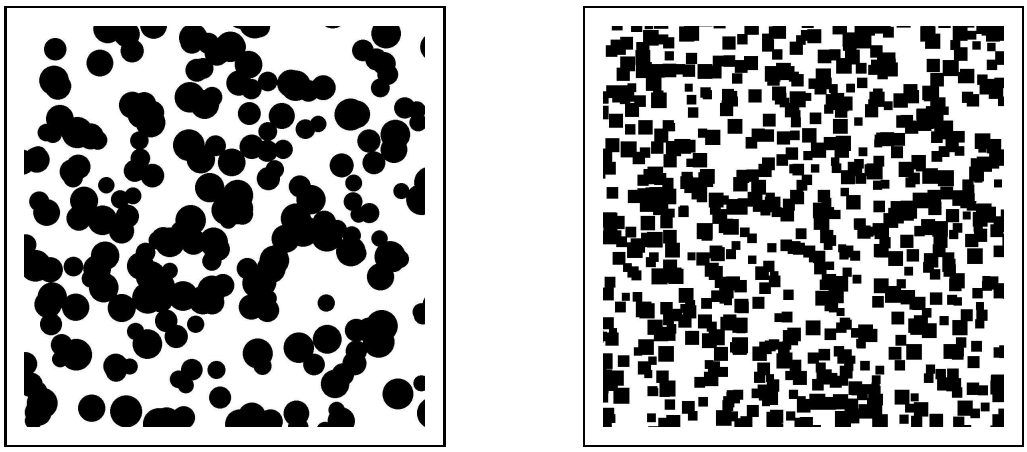

(a) (b)

Fig. 7. Realizations of a Boolean model with (a) circular and (b) square primary grains.

$r_0 = 5$, $r_{i+1} = r_i + 1.3$, $i = 0, \ldots, 49$ appear to perform pretty well in the case $W = [0, 1000]^2$ (run–time of 6 sec. per image, Pentium IV, 2.8 GHz). For $n > 50$ and larger radii, the run–time increases dramatically up to more then one hour. Due to minus sampling, the size of the radii is limited by the half of the diameter of the observation window W.

For the edge correction (20), a larger number $n \geqslant 1000$ of dilation radii can be used. For example, the following recursive rule yields good computational results together with a run–time of 0.2 sec. per image: $r_0 = 5000$, $r_{i+1} = r_i + 20.3$, $i = 0, \ldots, 999$. Note that the precision increases when using larger radii.

3.5 Numerical results

To compare the algorithms of Section 3.3 with those given in [5] and [19], two Boolean models with discs and squares as primary grains (cf. e.g. [27], [26], [30]) were used to generate the input images. For each Boolean model, 100 realizations were simulated in the window $W = [0, 1000]^2$. In this section, we estimate their specific intrinsic volumes. The intensity λ of the underlying Poisson point process of germs was chosen to match $\bar{V}_2(\Xi) = 0.5$. Explicit formulae for the specific intrinsic volumes of Boolean models can be found e.g. in [26] and [30]. They were used to compute the reference values $\bar{V}_2(\Xi), 2\bar{V}_1(\Xi), \bar{V}_0(\Xi)$.

For the Boolean model Ξ of discs whose radii are continuously uniformly distributed on $(20, 40)$, the intensity $\lambda = 2.36395286 \cdot 10^{-4}$ was chosen; see Figure 7 (a). The reference values are $\bar{V}_2(\Xi) = 0.5$, $2\bar{V}_1(\Xi) = 0.0222800$ and $\bar{V}_0(\Xi) = 3.919529 \cdot 10^{-5}$. The corresponding estimation results are shown in Table 5. For the Boolean model Ξ with the square primary grain whose side

length is discretely uniformly distributed on $[20, 40]$, the intensity was set to $\lambda = 7.4001478 \cdot 10^{-4}$; see Figure 7 (b). The reference values are $\bar{V}_2(\Xi) = 0.5$, $2\bar{V}_1(\Xi) = 0.044400887$ and $\bar{V}_0(\Xi) = 1.23577546 \cdot 10^{-4}$. The estimation results for this Boolean model are shown in Table 6. The realizations of the Boolean models were simulated in the Euclidean space and then discretized on the grid with lattice mesh size $\Delta = 1$.

In general, the estimation results for $\bar{V}_2(\Xi)$ and $\bar{V}_1(\Xi)$ are more precise than the results for $\bar{V}_0(\Xi)$. This phenomenon is also well known in the literature. Methods (iii) and (iv) differ mainly in their run–times. Edge correction (20) is much faster than minus sampling.

The estimated value 0.5011 of the area fraction in Table 5 is due to the natural fluctuations of the realizations of the Boolean model. Thus, it does not contradict the unbiasedness of the method (ii). For larger sequences of images the estimation results become better because of the law of large numbers.

For the estimation method (v) various exploratory point designs can be used; see e.g. [32]. In most cases, a rectangular lattice showed good results. A *Fibonacci–type* lattice leads to the same results with a slight increase of the computational variance. Another widely used point pattern is the so called *randomized Vienna coffeehouse design*. The results are good on average, but the variance is about twice as high as for other point designs. In Tables 5–6 calculations are made using a quadratic lattice of points $\{x_{ik}\}$ of mesh size 10.

4 Discussion

As it is clear from Table 2, the best performance (both in precision and run times) for the computation of intrinsic volumes of a deterministic polyconvex set is shown by the algorithms based on the inclusion–exclusion formula and on the Steiner formula. A weak point of the latter algorithm is surely the use of elementary pixel configurations with 3^d neighboring pixels (voxels) in $\mathbb{R}^d$, compare [18]. For $d \geqslant 3$, this results in a dramatic increase of the number of possible voxel configurations which leads to a longer run–time. On the contrary, the algorithm described in Section 2 uses elementary configurations of 2^d pixels (voxels) with acceptable run–time. One more advantage of this algorithm is its universality, i.e., it is applicable to any dimension with slight changes.

For isotropic (i.e., motion invariant) random closed sets such as the Boolean model of discs, Table 5 shows that the best results are achieved by the method (i). Methods (ii)–(v) yield similar results with an acceptable precision. Smallest variances of results are demonstrated by method (i). If the random closed set

Table 4
Overview of the methods used in Tables 5–6

Method	based on
(i)	paper [19, Section 8] by Mrkvička and Rataj
(ii)	books [9] by Serra and [5] by Ohser and Mücklich
(iii)	Steiner formula with minus sampling (using random fields (18))
(iv)	Steiner formula with alternative edge correction (20)
(v)	principal kinematic formula (using random fields (19))

Table 5
Results for the Boolean model with discs as primary grains

Algorithm	(i)	(ii)	(iii)	(iv)	(v)
$\widehat{V}_2(\Xi)$	—	0.5011	—	—	0.4903
δ	—	0.22%	—	—	-1.94%
Var $\cdot 10^4$	—	7.1005	—	—	8.8878
$2\widehat{V}_1(\Xi)$	0.0223	0.0221	0.0218	0.0241	0.0234
δ	0.00%	-0.95%	-2.28%	8.35%	4.87%
Var $\cdot 10^7$	4.9667	5.4412	7.6105	6.4811	11.2925
$\widehat{V}_0(\Xi) \cdot 10^5$	3.9195	1.3035	2.7402	1.6686	1.4357
δ	0.00%	-66.74%	-30.09%	-57.43%	-63.37%
Var $\cdot 10^{10}$	0.5893	1.3567	1.7951	1.3439	2.5404

Table 6
Results for the Boolean model with squares as primary grains

Algorithm	(i)	(ii)	(iii)	(iv)	(v)
$\widehat{V}_2(\Xi)$	—	0.50	—	—	0.4759
δ	—	0.00%	—	—	-4.82%
Var $\cdot 10^4$	—	1.951	—	—	2.2729
$2\widehat{V}_1(\Xi)$	0.0408	0.0412	0.0407	0.0438	0.0433
δ	-8.2%	-7.19%	-8.42%	-1.42%	-2.47%
Var $\cdot 10^7$	6.8933	7.2355	5.7038	8.1127	15.1922
$\widehat{V}_0(\Xi) \cdot 10^4$	1.4469	1.011	1.2963	1.1178	1.0765
δ	17.1%	-18.19%	4.9%	-9.55%	-12.89%
Var $\cdot 10^{10}$	1.4812	1.5529	1.9203	1.435	2.0614

is anisotropic (see Figure 7 (b) for the Boolean model of anisotropic squares), algorithms (iii)–(v) perform equally well. Worse results are shown by methods (i) and (ii). One should notice that Tables 5 and 6 can not be used to judge the absolute precision of different algorithms. These tables yield only the relative comparison of their performance.

Precise results of the method (i) in the case of the Boolean model of discs can be explained by a particular choice of dilation radii that fit circular grains best. For other grain shapes, the bias of this method can lead to greater relative errors. This disadvantage is partially compensated by the simplicity of the algorithm and small estimation variances. The exactness of method (i) seems to increase with increasing the area fraction of the random set Ξ. Vice versa, the exactness of methods (iii)–(v) might decrease. The reason for that lies, roughly speaking, in the dilation operation that is applied to the set Ξ itself in methods (iii)–(v) and to the complement of a small parallel set of Ξ in (i).

If the comparison of binary images on the basis of a central limit theorem of [20] is desirable, the use of methods (iii)–(v) is inevitable due to the nice asymptotic properties of the corresponding estimators. For other methods, such properties are still not known.

The best run–times (0.2 sec., 0.12638 sec., 0.1935 sec. per 1000×1000 image) are shown by the methods (i), (ii) and (iv), respectively. As in the deterministic case, the latter method is not so fast in three dimensions and does not admit an extension to higher dimensions which can be implemented.

Acknowledgements

We would like to thank J. Rataj and T. Mrkvička for the discussions that helped to improve the paper. Furthermore, we are indebted to T. Mrkvička for the results of method (i) that he kindly put at our disposal. Finally, we are grateful to the referees for their helpful comments.

References

[1] L. A. Santalo, Integral geometry and geometric probability, Addison Wesley, Reading, Massachusetts, 1976.

[2] V. Martinez, E. Saar, Statistics of the Galaxy Distribution, Chapman & Hall, Boca Raton, 2002.

[3] K. Mecke, D. Stoyan, Statistical Physics and Spatial Statistics, Vol. 554 of Lect. Notes Physics, Springer, Berlin, 2000.

[4] K. Mecke, D. Stoyan, Morphology of Condensed Matter, Vol. 600 of Lect. Notes Physics, Springer, Berlin, 2002.

[5] J. Ohser, F. Mücklich, Statistical Analysis of Microstructures in Materials Science, J. Wiley & Sons, Chichester, 2000.

[6] T. Mattfeldt, H.-W. Gottfried, H. Wolter, V. Schmidt, H. Kestler, J. Mayer, Classification of prostatic carcinoma with artificial neural networks using comparative genomic hybridization and quantitative stereological data, Pathology - Research and Practice 199 (12) (2003) 773–784.

[7] M. Ochs, J.-R. Nyengaard, A. Jung, L. Knudsen, M. Voigt, T. Wahlers, J. Richter, H.-J. Gundersen, The number of alveoli in the human lung, Am. J. Respir. Crit. Care Med. 196 (1) (2004) 120–124.

[8] Z. Tabor, Analysis of the influence of image resolution on the discriminating power of trabecular bone architectural parameters, Bone 34 (1) (2004) 170–179.

[9] J. Serra, Image Analysis and Mathematical Morphology, Academic Press, London, 1982.

[10] W. Nagel, J. Ohser, K. Pischang, An integral–geometric approach for the Euler–Poincaré characteristic of spatial images, Journal of Microscopy 189 (2000) 54–62.

[11] V. Robins, Computational topology for point data: Betti numbers of α–shapes, in: K. Mecke, D. Stoyan (Eds.), Morphology of Condensed Matter, Vol. 600 of Lect. Notes Physics, Springer, Berlin, 2002, pp. 261–274.

[12] V. Schmidt, E. Spodarev, Joint estimators for the specific intrinsic volumes of stationary random sets, Stochastic Process. Appl. 111 (2005) 959–981.

[13] E. Spodarev, V. Schmidt, On the local connectivity number of stationary random closed sets, in: C. Ronse, L. Najman, E. Decencière (Eds.), Proceedings of the 7th International Symposium on Mathematical Morphology, Springer, Dordrecht, 2005, pp. 343–356.

[14] J. Rataj, Estimation of intrinsic volumes from parallel neighborhoods, Rend. Circ. Mat. Palermo Suppl. (2006), to appear.

[15] H. Vogel, Digital unbiased estimation of the Euler–Poincaré characteristic in different dimensions, Acta Stereologica 16 (1997) 97–104.

[16] J. Ohser, W. Nagel, K. Schladitz, The Euler number of discretized sets – on the choice of adjacency in homogeneous lattices, in: K. Mecke, D. Stoyan (Eds.), Morphology of Condensed Matter, Vol. 600 of Lect. Notes Physics, Springer, Berlin, 2002, pp. 275–298.

[17] J. Ohser, W. Nagel, K. Schladitz, The Euler number of discretized sets – surprising results in three dimensions, Image Analysis and Stereology 22 (2003) 11–19.

[18] S. Klenk, V. Schmidt, E. Spodarev, A new algorithmic approach for the computation of Minkowski functionals of polyconvex sets, Computational Geometry: Theory and Applications 34 (3) (2006) 127–148.

[19] T. Mrkvička, J. Rataj, On estimation of intrinsic volume densities of stationary random closed sets, Preprint No. MATH-MU-2005/1, Charles University, Prague, submitted (2005).

[20] U. Pantle, V. Schmidt, E. Spodarev, A central limit theorem for functionals of germ–grain models, Adv. Appl. Probab. 38 (1) (2006) 76–94.

[21] R. Schneider, Convex Bodies. The Brunn–Minkowski Theory, Cambridge University Press, Cambridge, 1993.

[22] D. A. Klain, G.-C. Rota, Introduction to Geometric Probability, Cambridge University Press, Cambridge, 1997.

[23] R. Schneider, W. Weil, Integralgeometrie, B. G. Teubner, Stuttgart, 1992.

[24] H. Freeman, Computer processing of line drawing images, ACM Comput. Surveys 6 (1) (1974) 57–98.

[25] J. Mayer, A time-optimal algorithm for the estimation of contact distribution functions of random sets, Image Analysis & Stereology 23 (11) (2004) 177–183.

[26] D. Stoyan, W. S. Kendall, J. Mecke, Stochastic Geometry and its Applications, 2nd Edition, J. Wiley & Sons, Chichester, 1995.

[27] G. Matheron, Random Sets and Integral Geometry, J. Wiley & Sons, New York, 1975.

[28] A. J. Baddeley, Spatial sampling and censoring, in: O. Barndorff-Nielsen, W. Kendall, M. N. M. Lieshout (Eds.), Stochastic Geometry. Likelihood and computation, Vol. 80 of Monographs on Statistics and Applied Prpobability, Chapman & Hall, Boca Raton, 1999, Ch. 2, pp. 37–78.

[29] J. P. Jernot, P. Jouannot-Chesney, C. Lantuejoul, Local contributions to the Euler–Poincaré characterisitic of a set, J. Microscopy 215 (2004) 40–49.

[30] R. Schneider, W. Weil, Stochastische Geometrie, Teubner Skripten zur Mathematischen Stochastik, Teubner, Stuttgart, 2000.

[31] W. Weil, J. A. Wieacker, Densities for stationary random sets and point processes, Adv. Appl. Probab. 16 (1984) 324–346.

[32] W. G. Müller, Collecting Spatial Data, Physica–Verlag, Heidelberg, 2001.